Received 8 September 2021; revised 3 November 2021; accepted 13 November 2021. Date of publication 7 December 2021;
date of current version 5 January 2022.

Digital Object Identifier 10.1109/OJAP.2021.3133470

Photonics-Based Near-Field Measurement and Far-Field Characterization for 300-GHz Band Antenna Testing

YUSUKE TANAKA[1] (Graduate Student Member, IEEE), GUILLAUME DUCOURNAU[2], CYBELLE BELEM-GONCALVES[3], FRÉDÉRIC GIANESELLO[3] (Member, IEEE), CYRIL LUXEY[4] (Fellow, IEEE), ISSEI WATANABE[5], AKIHIKO HIRATA[7] (Senior Member, IEEE), NORIHIKO SEKINE[6] (Member, IEEE), AKIFUMI KASAMATSU[5], AND SHINTARO HISATAKE[1], (Member, IEEE)

[1]Electrical and Energy System Engineering Division, Faculty of Engineering, Gifu University, Gifu 501-1193, Japan

[2]Institute of Electronics Microelectronics and Nanotechnologies, UMR CNRS 8520, University of Lille, 59000 Lille, France

[3]TR&D/STD/iDNA/RF Support & Services, STMicroelectronics, 38926 Crolles, France

[4]Polytech'Lab, Polytech Nice-Sophia, University of Cote d'Azur, 06903 Sophia Antipolis, France

[5]Advanced ICT Research Institute, National Institute of Information and Communications Technology, Koganei 184-8795, Japan

[6]Terahertz Laboratory, Terahertz Technology Research Center, National Institute of Information and Communications Technology, Koganei 184-8795, Japan

[7]Faculty of Engineering, Chiba Institute of Technology, Narashino 275-0016, Japan

CORRESPONDING AUTHOR: S. HISATAKE (e-mail: shintaro.hisatake@gmail.com)

This work was supported in part by the Horizon 2020, the European Union's Framework Program for Research and Innovation under Grant 814523.
ThoR has also received funding from the National Institute of Information and Communications Technology in Japan.

ABSTRACT In this study, photonics-based near-field measurement and far-field characterization in a 300-GHz band are demonstrated using an electrooptic (EO) sensor with planar scanning. The field to be measured is up-converted to the optical domain (1550 nm) at the EO sensor and delivered to the measurement system with optical fiber. The typical phase drift of the system is 0.46° for the one-dimensional measurement time of 13 s, which is smaller than the standard deviation of the phase measurement of 1.2° for this time scale. The far-field patterns of a horn antenna calculated from the measured near-field distribution are compared with that measured with the direct far-field measurement system using a vector network analyzer. For the angular related parameters, the accuracy of the results obtained by our near-field measurement are comparable to that of those obtained by direct far-field measurements. The sidelobe level discrepancy (approximately 1 dB) between the results obtained based on our near-field measurement and those from the direct far-field measurements are attributed to the excess noise of the probe correction data. We believe that photonics-based near-field measurements with spherical EO probe scanning will pave the way for the characterization of high-gain antennas at the 300-GHz band.

INDEX TERMS EO probe, far-field characterization, near-field measurement, photonics technology, planar scanning, 300 GHz.

I. INTRODUCTION

IN RECENT years, the development of antennas operating in the upper limit of the millimeter-wave band or the lower limit of the terahertz (THz) band has become increasingly important due to the increasing need for high-capacity and -speed wireless communications in these frequency bands. The spectral range of approximately 300 GHz is expected to realize high-capacity and ultra-fast wireless communication using a large amount of the bandwidth that are several tens of GHz [1], [2]. In the past years, transmission experiments in accordance with the IEEE802.15.3d standard [3] have been actively conducted using several types of antennas [4]–[8]. Accordingly, a variety of antennas operating in the 300-GHz band has been proposed and demonstrated [4], [5], [8], [9]. Antennas with a high gain of approximately 40-50 dBi are being considered for use in backhaul/fronthaul applications

for a distance of over several hundred meters [10]. Although the gain is low at approximately 15 dBi, an antenna that can be installed on mobile devices with dimensions about the size of a wavelength has also been demonstrated, aiming at device-to-device communications and kiosk application, among others [9]–[12]. Horn antennas with a moderate gain of approximately 25 dBi have been routinely used in laboratory environment transmission experiments [13], [14]. The need to establish the antenna characterization technique in the 300-GHz band is urgent.

The antenna radiation pattern characterization can be broadly classified into three methods: far-field measurement (FFM), compact antenna test range (CATR); and near-field measurement (NFM) [15]. Among them, the NFM technique is the key in the 300-GHz band. For higher-gain antennas, FFMs require huge, unrealistic test sites for antenna characterizations because the distance (d) between the antenna under test (AUT) and the probe antenna must be at least $d = 2D^2/\lambda$, where D and λ are the diameter of the AUT and the wavelength, respectively. For example, d reaches approximately 58 m at 340 GHz for a Cassegrain antenna (used in indoor transmission experiments with 50.0 m transmission distance) with an antenna gain of 48.4 dBi and a D of 160 mm [10]. CATRs are a good alternative to overcome this limitation [16]. However, the measurement accuracy of CATRs is affected by various factors, including feed pattern, surface tolerance, and edge treatment of the collimating reflector used in the measurement system [17]; therefore, a sophisticated system design and the accurate manufacturing of the large collimating reflector are required [18], [19]. In the NFM technique, the amplitude and the phase distribution of the field at the AUT vicinity are sampled with a probe antenna. In most cases, it is an open-ended waveguide (OEW), and the far-field characteristics are derived using numerical methods [20]. The test site can be compact, regardless of the antenna diameter. It also enables a higher signal-to-noise ratio (SNR) measurement. However, due to the close proximity of the AUT and the OEW, the mutual coupling between them significantly affects the measurement accuracy. The effect of the OEW should be de-embedded from the far-field pattern of the AUT using the probe correction technique [21]–[24]. In addition, scattering from devices directly connected to the OEW (e.g., mixers) and electrical cables can easily exacerbate the situation. Accordingly, probe correction and a careful consideration of the measurement system design to reduce scattering from metallic components are needed for an accurate measurement.

This study presents a photonics-based NFM system at the 300-GHz band using all dielectric electrooptic (EO) sensors. The EO sensor connected to the optical fiber contains no metallic elements. The radiofrequency (RF) field to be measured is up-converted to the optical domain (1550 nm) at the EO sensor and delivered to the measurement system with optical fiber. Our system has the following features over conventional systems: (1) the probe head is small (submillimeter order), and all the components, including the optical fiber,

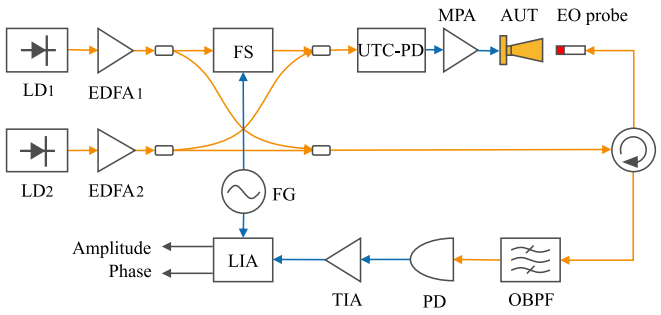

FIGURE 1. Schematic of a photonics-based NFM system. LD: laser diode; FS: frequency shifter; UTC-PD: unitraveling-carrier photodiode; MPA: medium power amplifier; AUT: antenna under test; EDFA: erbium-doped optical amplifier; OBPF: optical band pass filter; PD: photodiode; TIA: transimpedance amplifier; and LIA: lock-in amplifier.

are made of dielectric material; hence, the field disturbance to be measured is negligible; (2) the probe head is extremely light; thus, the deflection of the scanner that holds the probe is negligible, enabling a high-fidelity pattern measurement; (3) the detected signal is transmitted to the measurement system via flexible and low-loss optical fibers; therefore, the system can easily accommodate large scan areas; and (4) the local oscillator (LO) signal is generated based on the photonics-based self-heterodyne technique [25], and the RF signal is detected based on a nonpolarimetric frequency down-conversion technique [26], which is more stable than the conventional polarimetric technique [27]. Thus, it can cover several hundreds of GHz frequency band with a high phase detection accuracy without changing the EO probe head [28]–[31]. In this study, we measure the near-field of a horn antenna based on planar scanning. We then calculate the far-field pattern with probe sensitivity correction and compare it with the patterns measured with the FFM system using sources/direct-detection or the vector network analyzer (VNA) technique. The obtained far-field distribution very well agree with each other. The results suggest that accurate radiation patterns can be measured by the NFM system without any probe correction if spherical scanning is used.

II. MEASUREMENT SYSTEM

A. NFM SYSTEM

Fig. 1 shows the photonics-based NFM system based on the self-heterodyne and nonpolarimetric frequency down-conversion techniques. The orange line represents the optical fiber, while the blue line represents the electrical cable. The RF and LO signals were generated using two free-running 1550 nm laser diodes (LDs). Although the RF signal frequency fluctuated due to the free-running laser, both the amplitude and the phase distribution were visualized based on the self-heterodyne technique. The LD frequencies were set as f_1 and f_2 ($f_2 > f_1$) and combined using polarization maintaining fiber (PMF) couplers to produce a beat note at a frequency of $f_{THz} = f_2 - f_1 - f_s$ for the THz wave generation (RF signal generation). Here, an EO frequency shifter was used to shift the optical frequency of the LD_1 (f_1) by f_s (typically 100 kHz to 10 MHz) for the self-heterodyne detection. A high-speed photodiode (PD), such as a unitraveling-carrier

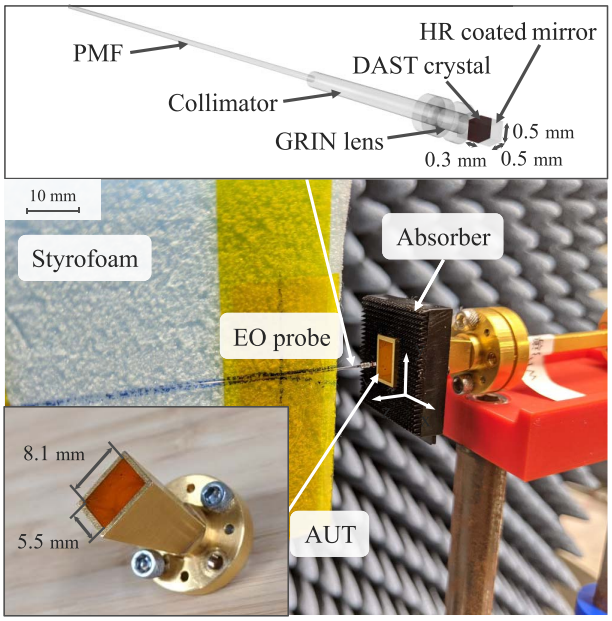

FIGURE 2. Configuration of the EO probe and photo of the measurement setup around AUT. DAST: 4-N,N-dimethylamino-4-N-methyl stilbazolium tosylate; PMF: polarization maintaining fiber; HR: high reflection; GRIN: graded-index.

PD (UTC-PD), can be used as an O/E converter for the RF generation. An optical beat note considered as the LO signal was used as a probe beam for the nonpolarimetric EO frequency down-conversion. The LO signal was modulated by the RF signal to be detected in the EO crystal. Modulation sidebands corresponding to the frequency up-converted RF signal were then generated. The upper sideband and the f_2 component of the LO signal were simultaneously extracted by the optical bandpass filter and detected by a low-speed PD. The frequency down-converted signal corresponding to the intermediate frequency (IF) signal was amplified by the transimpedance amplifier and supplied to the lock-in amplifier. The measured amplitude and phase data were acquired by a personal computer.

Fig. 2 shows the EO probe configuration and a photo of the measurement setup around the AUT. We employed a standard rectangular-type horn antenna (WR-3.4: 220-330 GHz) as the AUT. As shown in Fig. 2 inset, the antenna aperture size was 8.1 mm × 5.5 mm. The EO probe was made of dielectric materials without any metallic components. The EO crystal was a DAST (4-N,N-dimethylamino-4-N-methyl stilbazolium tosylate) crystal. The EO crystal dimension was approximately 0.5 mm × 0.5 mm × 0.3 mm. The EO crystal was attached to the gradient index lens (GRIN lens) and PMF. On the other side, a high-reflection dielectric mirror was attached to the EO crystal. The probe beam output from the PMF was collimated by the GRIN lens, traveled inside the EO crystal, and then reflected back to the PMF. The probe beam interacted with the RF signal in the EO crystal to generate the modulation sidebands. No metallic antennas on the EO crystal minimized the scattering by the probe head. The optical fiber also drastically reduced the scattering compared with the conventional probe antenna,

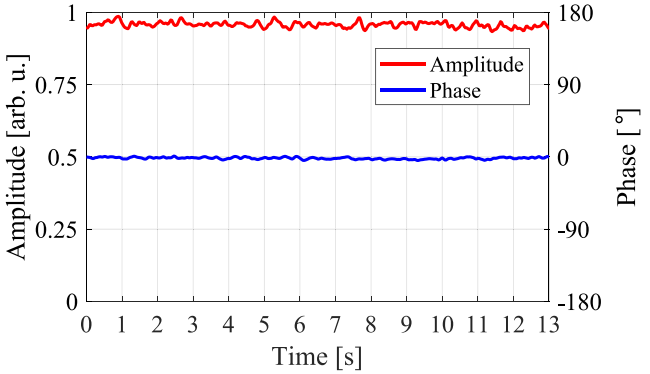

FIGURE 3. Stability of the detection: the red line the indicates detected amplitude data, and the blue line indicates the detected phase data.

in which a metallic cable or a waveguide is used. The EO probe had a sensitivity axis along the a-axis of the DAST crystal. The cross-polarization suppression ratio of the EO probe was approximately 22 dB. The EO probe was fixed to styrofoam with insulation tape, which was attached to the automated stage such that the EO probe was away from the metallic components. The stage was a Sigma Koki linear motion stage (SG SP26-300), with a resolution of 4 μm and positioning accuracy of 15 μm. The relative position of the EO probe and antenna was adjusted via monitoring them with a camera so that the scanning plane was parallel to the horn antenna aperture.

B. EVALUATION OF THE MEASUREMENT SYSTEM

Fig. 3 shows the stability of the amplitude and phase detection of our system. In this experiment, the probe was fixed at the center of the antenna surface. A 286-GHz RF signal was generated using UTC-PD and detected by the EO probe. The output power of UTC-PD was −14 dBm. The MPA gain was 15 dB. The horizontal axis of the graph is time in second, and the vertical axis is normalized amplitude and phase in degree. The amplitude was normalized to its maximum value. The phase was offset to 0° from the initial phase. The lock-in time constant was 30 ms. We measured the amplitude and the phase for 13 s, which corresponded to the typical measuring time for a one-dimensional (1D) probe scan in the NFM. The SNR of the amplitude measurement was $20log(S/N) = 40.2$ dB, where S is the mean amplitude, and N is the standard deviation of the measured amplitude data. The standard deviation of the phase measurement was 1.2°.

The detection sensitivity of the EO probe varied depending on the direction of the incoming electric field. For an accurate evaluation of the antenna far-field distribution, the angular characteristic of the probe sensitivity must be measured, and the far-field distribution must be corrected based on the measured probe sensitivity characteristics. Fig. 4 shows the angular sensitivity characteristic measurement setup. The plane wave was generated by placing the Teflon lens at a 67 mm distance from the horn antenna. The EO probe was located 10 mm from the Teflon lens. The antenna and the Teflon lens were fixed on an automatic rotation stage. We used

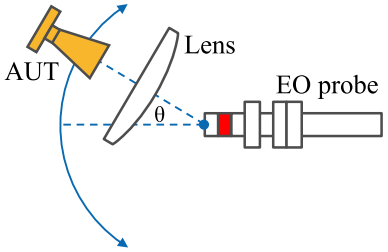

FIGURE 4. Schematic of the experimental configuration for the angular sensitivity measurement of the EO probe.

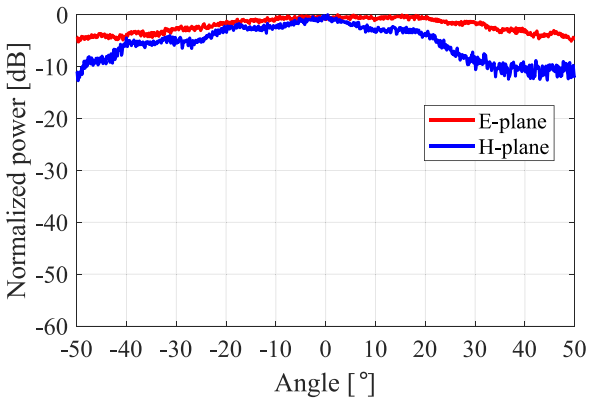

FIGURE 5. Angular sensitivity characteristics of the EO probe: the red line depicts the characteristic along the E-plane,while the blue line represents the characteristic along the H-plane.

Sigma Koki Co. OS MS-60YAW for the rotation stage. The resolution was 0.005°, and the positioning accuracy was 0.1°. The sensitivity characteristics were measured by changing the incident angle of the plane wave along the E- and H-planes. Fig. 5 illustrates the measured angular characteristics of the EO probe. The red line represents the characteristic along the E-plane, while the blue line displays the characteristic along the H-plane. The sensitivity decreased as the angle increased. The 3 dB bandwidth were approximately 58° and 20° in the E- and H-planes, respectively. Note that the strange properties along the H-plane at a higher angle were presumed to be caused by crystal imperfections, although further research is needed to understand this.

C. NFM ALGORITHM

Fig. 6 shows the schematic of the two-dimensional (2D) NFM procedure. The xy plane at 2 mm from the antenna surface was measured. The EO probe moved along the red arrow (Pass (1)) for the 2D measurement of the amplitude and phase distribution. The measurement area was 11 mm × 13 mm. The EO probe moved along the x-axis for 11 mm with 0.1 mm interval. Subsequently, the EO probe moved along the y-axis for 0.1 mm and moved back to the negative direction along the x-axis with 0.1 mm interval. The one-line measurement along the x-axis lasted for approximately 13 s. As shown in Fig. 3, the phase drift is smaller than the standard deviation of the phase measurement (1.2°) within the one-line measurement time of 13 s. In contrast, the 2D measurement was completed after approximately 30 min. We observed the phase drift for the

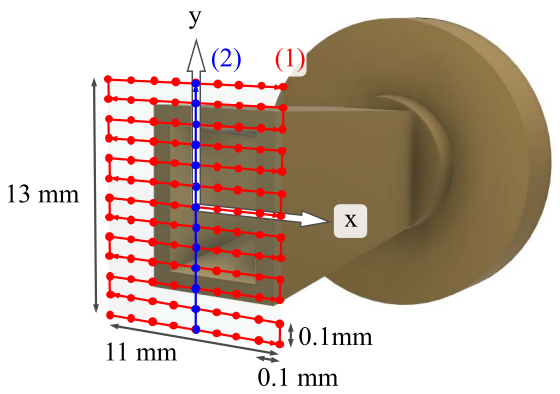

FIGURE 6. Schematic of the measurement procedure. The EO probe moves along the red arrow (Pass (1)) for the 2D near-field distribution measurement. The longterm phase drift is canceled using the phase distribution measured along the blue arrow (Pass (2)).

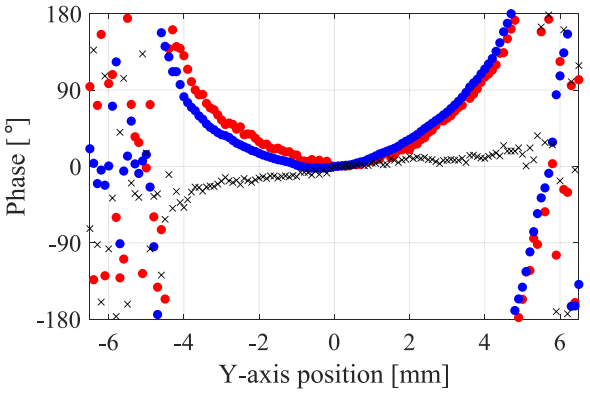

FIGURE 7. Phase distribution along the y-axis. Red dots: extracted from the measured 2D distribution (Pass (1) measurement). Blue dots: measured along the y-axis (Pass (2) measurement). Cross marks: the difference between the red and blue dots.

30-min measurement. Fig. 7 compares the phase distribution along the y-axis extracted from the measured 2D distribution (red dots: Pass (1) measurement) and the 1D phase data along the y-axis (blue dots: Pass (2) measurement) measured immediately after Pass (1) measurement. The cross marks represent the difference between the two data. We observed a phase drift of 2.1°/min. This longterm phase drift can be compensated for using the 1D phase data along the y-axis measured immediately after the 2D measurement as the phase reference for each 1D phase distribution along the x-axis. The amplitude distribution was also compensated for using the 1D amplitude data along the y-axis to eliminate the longterm amplitude drift.

III. RESULTS AND DISCUSSION

We ignored the cross-polarization component because AUT, which is the horn antenna, emits a linearly polarized RF field, and the EO probe has 22 dB of cross-polarization suppression ratio [32]. The near-field was measured by aligning the a-axis of the DAST crystal to the principal polarization of the RF field to be measured. Fig. 8 shows the measured 2D amplitude and phase distribution. The horn antenna in this figure is the polygon data (i.e., the 3D model and the

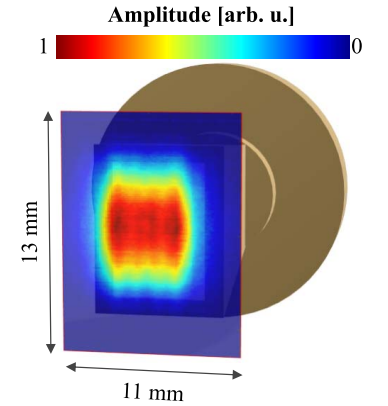

(a) Amplitude

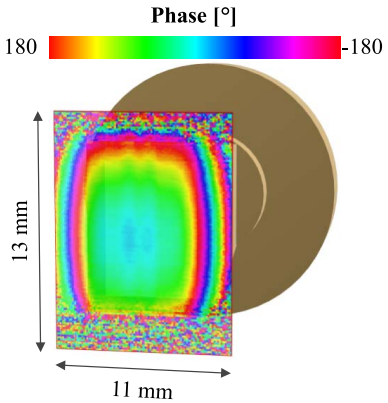

(b) Phase

FIGURE 8. Measured near-field distributions (frequency: 286 GHz): (a) amplitude distribution normalized to its maximum value; (b) phase distribution measured in degree. The data were measured five times and averaged.

experimental results were put together to show the field distribution). The frequency was 286 GHz. The measurement area was 11 mm × 13 mm, with a 0.1 mm measurement grid. The time constant of the lock-in detection was 30 ms. The total measurement time was approximately 30 min. The phase drift that occurred during the measurement was compensated for, as described in the Section II-C. The maximum SNR of 40 dB was obtained at the center of the antenna aperture. The amplitude data were normalized to their maximum values in the measured plane. Notably, our current system is a single-polarization measurement system. The orthogonal component can be measured by rotating the probe by 90°.

Fig. 9 depicts the 3D representation of the 2D far-field pattern. 2D far-field pattern calculated from the measured near-field distribution shown in Fig. 8. The calculation was based on the 2D Fourier transform of the near-field distribution [20]. The horn antenna in this figure was also the polygon data. We extracted the 1D far-field distribution in the E- and H-planes from the 2D far-field data to evaluate the standard error in the far field distribution (Fig. 10). In these far-field patterns, the angular characteristics of the probe sensitivity were not compensated for, that is, these were raw data. The radiation pattern results are known to be

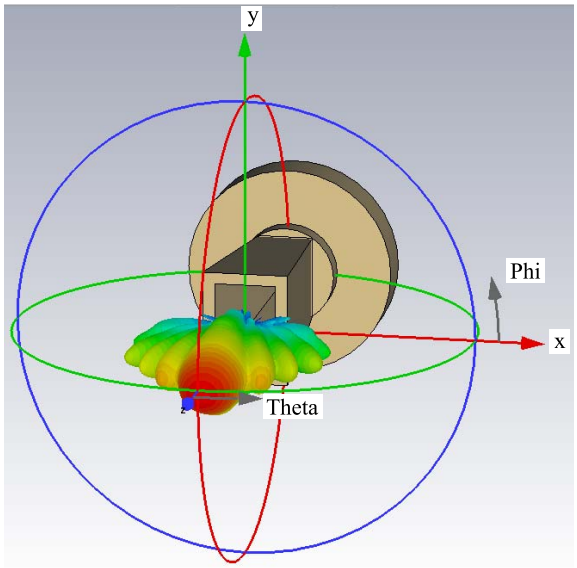

(a)

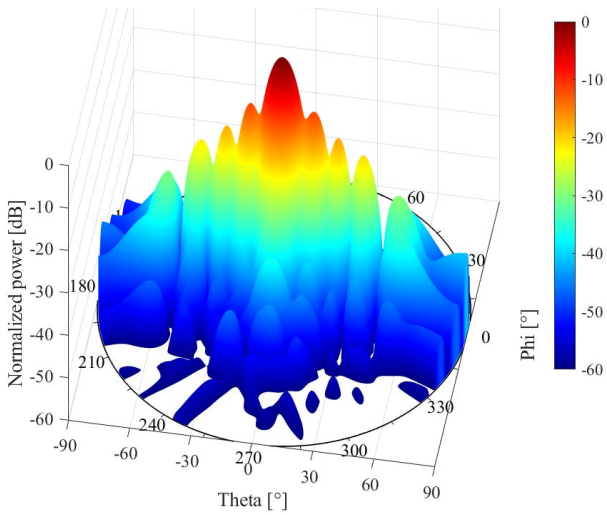

(b)

FIGURE 9. 3D representation of the 2D far-field pattern calculated from the measured 2D near-field distribution. (a) Far-field pattern with the antenna CAD data, and (b) representation in a Cylindrical coordinate system.

valid within the angular range of θ defined as follows from the test antenna shape and the measurement plane [33]:

$$\theta = \arctan \frac{L - a}{2d}, \tag{1}$$

where, L is the maximum width of the measurement plane; a is the maximum aperture of the AUT; and d is the distance between the AUT aperture and the measurement plane. In our case, $L = 11$ and 13 mm, and $a = 5.5$ and 8.1 mm for the E- and H-planes, respectively, and $d = 2$ mm. Using these values, the effective angular ranges of the E- and H-planes were calculated as 54.0° and 50.8°, respectively. Therefore, the radiation pattern shown in Fig. 10 was limited within ±50°.

NFMs were repeated five times. The error bars in the far-field distribution were then calculated. The radiation

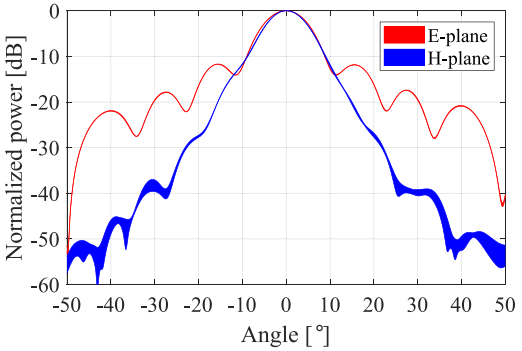

FIGURE 10. Measured 1D far-field distribution in the E- and H-planes extracted from the 2D far-field distribution. The EO probe sensitivity was not compensated for.

patterns in Fig. 10 were drawn by changing the line thickness according to the standard errors (SEs) of the five-time measurement results. In the E-plane characteristic, precise measurements were repeated, and the maximum SE was 0.8 dB. Meanwhile, a relatively large SE was obtained at a higher angular position in the H-plane characteristic. The SEs at +10°, +20°, +30°, +40°, and +50° corresponded to 0.08, 0.23, 1.28, 1.55, and 1.85 dB, respectively. The relatively large error bar in the H-plane at the higher angle was caused by the relatively lower sensitivity of the EO probe in this direction (Fig. 4).

We then compared the results of the radiation pattern measured using our system and those of the FFM systems at 286 GHz. We conducted two distinct direct FFMs, in which the OEW probe or conical horn antenna was placed at the far-field region (Fig. 11). The first one uses a set of sources/direct-detection (Fig. 11(a)) was conducted at the Institute of Electronics, Microelectronics and Nanotechnology of National Center for Scientific Research (IEMN-CNRS), France. The AUT was fixed, and the conical horn antenna with a Schottky diode was scanned on a spherical far-field. The distance between the AUT and the conical horn antenna was 0.2 m. The second one using the VNA technique (Fig. 11(b)) was conducted at the National Institute of Information and Communications Technology (NICT), Japan. Tx was fixed. The azimuth and elevation angles of Rx were rotated. The distance between Tx and Rx was 0.5 m. The angular resolutions of the IEMN-CNRS and NICT measurements were 1° and 0.1°, respectively. The power measurement error of 0.1 dB in both FFMs was limited by the VNA and the frequency extender.

Fig. 12 presents a comparison between three results. The positions of the main lobe peaks were aligned for a comparison. The blue line depicts the result obtained based on the NFM, while the red line displays that obtained based on the FFM using a set of sources/direct-detection. The black line illustrates the result obtained based on the FFM using the VNA technique. The angular characteristics of our EO probe were compensated for in this comparison. As shown in Fig. 12, the results obtained by our system agreed well with those obtained by the direct FFM based on conventional systems.

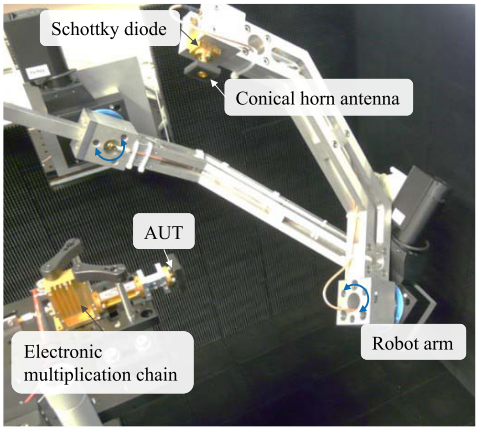

(a)

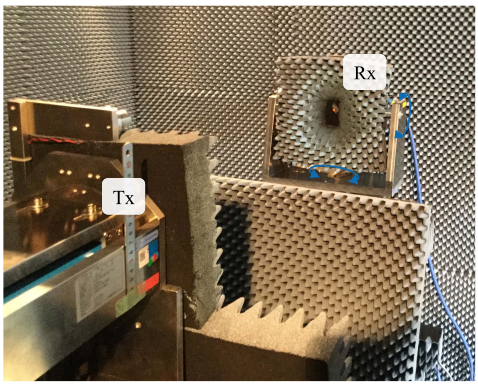

(b)

FIGURE 11. Schematic of the direct far-field measurement system (a) at IEMN-CNRS using a multiplication chain and a Schottky receiver and (b) at NICT using the VNA technique in the WR-3.4 band.

For a quantitative comparison, we summarized the far-field characteristics obtained based on the near-FFMs in Table 1. We compared the 3 dB beamwidth in the E- and H-planes and the levels and positions of the sidelobes in the E-plane. The sidelobe levels and positions are quantities relative to the mainlobe level and position, respectively. Fig. 13(a) presents the differences between the far-field characteristics obtained by the NFM and the FFM using a set of sources/direct-detection and that using the VNA. Fig. 13(a) shows the parameters related to the angle position. Fig. 13(b) depicts the parameters related to the level. The blue bars denote the comparisons between the NFM and the FFM using a set of sources/direct-detection. The red bars represent the comparison between the FFM using a set of sources/direct-detection and that using the VNA technique. The black bars are the comparison between the FFM using the VNA technique and the NFM. As shown in Table 1 and Figs. 13(a) and 13(b), level and position differences exist, even between the FFMs. Fig. 13(a) shows that either the differences between the NFM and the FFM using a set of sources/direct-detection (blue bars) or that between the NFM and the FFM using VNA technique (black bars) are smaller than those of the FFMs using a set of sources/direct-detection and the VNA technique (red bars). For the angle parameters, the accuracy

TABLE 1. Comparison of the measured far-field characteristics of AUT at 286 GHz. The data extracted from Fig. 12.

			NFM (compensated)	FFM (sources/direct-detection)	FFM (VNA technique)
E-plane	3 dB beamwidth [°]		9.6	10.9	9.6
	+1st sidelobe	position [°]	15.1	15	15.0
		level [dB]	-12.2	-10.9	-11.2
	-1st sidelobe	position [°]	-15.3	-15	-14.0
		level [dB]	-11.1	-11.2	-11.3
	+2nd sidelobe	position [°]	26.9	27	27.4
		level [dB]	-16.3	-16.2	-16.9
	-2nd sidelobe	position [°]	-28.0	-26	-27.5
		level [dB]	-15.7	-16.9	-16.8
	+3rd sidelobe	position [°]	40.6	40	-
		level [dB]	-18.2	-19.1	-
	-3rd sidelobe	position [°]	-40.7	-39	-
		level [dB]	-18.0	-18.7	-
H-plane	3 dB beamwidth [°]		9.5	9.4	9.6

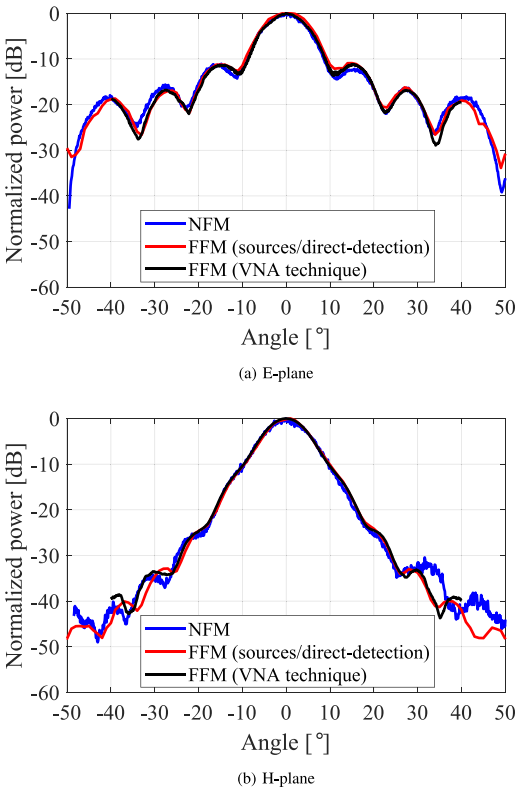

(a) E-plane

(b) H-plane

FIGURE 12. Comparison of the far-field results between the near- and far-field measurements using a set of sources/direct-detection and far-field measurements using the VNA technique.

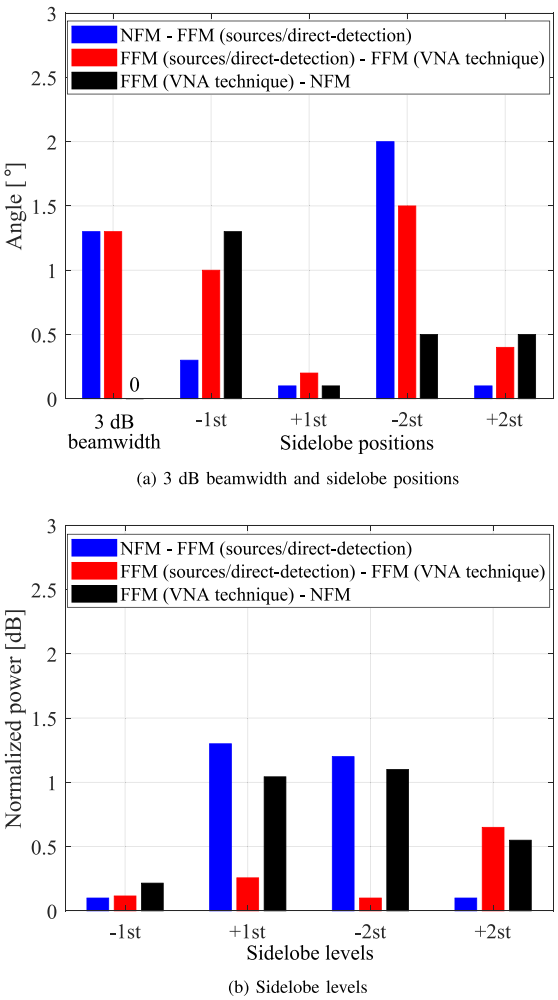

(a) 3 dB beamwidth and sidelobe positions

(b) Sidelobe levels

FIGURE 13. Differences between the far-field characteristics in the E-plane obtained by the near-and far-field measurement using a set of sources/direct-detection and far-field measurement using the VNA.

of the results obtained by our NFM was comparable to that of those obtained by the FFMs.

The maximum sidelobe level differences between the FFMs using a set of sources/direct-detection and VNA technique was 0.7 dB. Meanwhile, the sidelobe level differences between our NFM and the FFM using the VNA technique at the +1st and -2nd sidelobes were 1 and 0.9 dB, respectively. The SEs of our NFM at the position of the +1st and −2nd sidelobes were 0.05 and 0.04 dB, respectively. The angular sensitivity of the EO probe was compensated for by the relatively noisy experimental data shown in Fig. 5. The noise level of the compensation data in the E-plane at the +1st and −2nd sidelobe positions was roughly estimated as 0.7 dB, which limited the accuracy level in our calculated far-field patterns. The relatively large noise level of the probe compensation was caused by the low SNR (i.e., 28 dB) in the sensitivity characteristic measurement. The probe correction can be eliminated by employing spherical scanning [34]. We believe that photonics-based NFMs with spherical EO probe scanning will pave the way for the characterization of high-gain antennas at the 300-GHz band.

IV. CONCLUSION

We demonstrated herein the NFM and the far-field characterization at the 300-GHz band based on the photonics-based system using the EO probe. The typical phase drift of the system was 0.46° for the 1D measurement time of 13 s, which was smaller than the standard deviation of the phase measurement of 1.2° for this time scale. In our measurement procedure, the longterm phase drift was eliminated; therefore, the precise amplitude and phase distribution were measured. The far-field patterns of a horn antenna calculated from the measured near-field distribution with EO probe correction were compared with that measured with the direct FFM systems using a set of sources/direct-detection and the VNA technique. The results showed a good agreement between both. For the angle parameters (e.g., beamwidth and sidelobe position), the accuracy of the results obtained by our NFM were comparable to that of those obtained by the direct FFMs. The sidelobe level discrepancy of approximately 1 dB between the results obtained based on the NFM and the FFMs were caused by the excess noise of the probe correction data. We believe that photonics-based NFMs with spherical EO probe scanning will pave the way for characterizing high-gain antennas at the 300-GHz band.

ACKNOWLEDGMENT

The measurements conducted in Lille received support from IEMN UHD Flagship, SPATIOTERA ANR Project, MEL-I-site Teril-Waves, and DYDICO projects as well as CPER Photonics for Society. 300 GHz characterization steps are also supported by the ITN Marie-Curie "TERAOPTICS," funded under the E.U. Horizon 2020.

REFERENCES

[1] T. Kürner, "Turning THz communications into reality: Status on technology, standardization and regulation," in *Proc. 43rd Int. Conf. Infrared Millimeter THz Waves (IRMMW-THz)*, Nagoya, Japan, 2018, pp. 1–3.

[2] J. Machado *et al.*, "Wireless terahertz system applications for networks beyond 5G," Zelzate, Belgium, TERRANOVA Consortium, White Paper, Mar. 2019.

[3] *IEEE Standard for High Data Rate Wireless Multi-Media Networks–Amendment 2: 100 Gb/s Wireless Switched Point-to-Point Physical Layer*, IEEE Standard 802.15.3d-2017, 2017, pp. 1–55.

[4] B. Zhang *et al.*, "Metallic 3-D printed antennas for millimeter- and submillimeter wave applications," *IEEE Trans. THz Sci. Technol.*, vol. 6, no. 4, pp. 592–600, Jul. 2016.

[5] H. Wang, X. Dong, M. Yi, F. Xue, Y. Liu, and G. Liu, "Terahertz high-gain offset reflector antennas using SiC and CFRP material," *IEEE Trans. Antennas Propag.*, vol. 65, no. 9, pp. 4443–4451, Sep. 2017.

[6] K. Tekkouk *et al.*, "Corporate-feed slotted waveguide array antenna in the 350-GHz band by silicon process," *IEEE Trans. Antennas Propag.*, vol. 65, no. 1, pp. 217–225, Jan. 2017.

[7] S. Adibelli, P. Juyal, C.-L. Cheng, and A. Zajic, "Terahertz near-field focusing using a 3-D printed cassegrain configuration for backscattered side-channel detection," *IEEE Trans. Antennas Propag.*, vol. 67, no. 10, pp. 6627–6638, Oct. 2019.

[8] M. Alibakhshikenari *et al.*, "High-gain on-chip antenna design on silicon layer with aperture excitation for terahertz applications," *IEEE Antennas Wireless Propag. Lett.*, vol. 19, pp. 1576–1580, 2020.

[9] T. Tajima, H. J. Song, K. Ajito, M. Yaita, and N. Kukutsu, "300-GHz step-profiled corrugated horn antennas integrated in LTCC," *IEEE Trans. Antennas Propag.*, vol. 62, no. 11, pp. 5437–5444, Nov. 2014.

[10] C. Wang *et al.*, "0.34-THz wireless link based on high-order modulation for future wireless local area network applications," *IEEE Trans. THz Sci. Technol.*, vol. 4, no. 1, pp. 75–85, Jan. 2014.

[11] Y. Samura *et al.*, "High-gain and low-profile dielectric cuboid antenna at J-band," in *Proc. 14th Eur. Conf. Antennas Propag. (EuCAP)*, Copenhagen, Denmark, 2020, pp. 1–4.

[12] K. Yamada *et al.*, "Short-range wireless transmission in the 300 GHz band using low-profile wavelength-scaled dielectric cuboid antennas," *Front. Commun. Netw.*, vol. 2, p. 32, Jul. 2021.

[13] T. Nagatsuma, H.-J. Song, and Y. Kado, "Challenges for ultrahigh speed wireless communications using terahertz waves," *J. THz Sci. Technol.*, vol. 3, pp. 55–65, Jul. 2010.

[14] I. Dan, G. Ducournau, S. Hisatake, P. Szriftgiser, R.-P. Braun, and I. Kallfass, "A superheterodyne 300 GHz wireless link for ultra-fast terahertz communication systems," in *Proc. 49th Eur. Microw. Conf. (EuMC)*, Paris, France, 2019, pp. 734–737.

[15] J. Tuovinen, "Method for testing reflector antennas at THz frequencies," *IEEE Antennas Propag. Mag.*, vol. 35, no. 6, pp. 7–13, Dec. 1993.

[16] J. D. Huff and C. B. Brechin, "A millimeter compact range," in *Proc. IEE Colloquium Antenna Meas. Using Compact Antenna Test Range*, London, U.K., 1991, pp. 1–8.

[17] S. F. Gregson and C. G. Parini, "Examination of the effect of common CATR quiet zone specifications on antenna pattern measurement uncertainties," in *Proc. Loughborough Antennas Propag. Conf.*, 2017, p. 5.

[18] A. Lonnqvist *et al.*, "Hologram-based compact range for submillimeter-wave antenna testing," *IEEE Trans. Antennas Propag.*, vol. 53, no. 10, pp. 3151–3159, Oct. 2005.

[19] V. Viikari and A. V. Risnen, "Antenna pattern correction technique based on signal-to-interference ratio optimization," *IEEE Antennas Wireless Propag. Lett.*, vol. 6, pp. 267–270, 2007.

[20] C. A. Balanis, *Antenna Theory: Analysis and Design*, 2nd ed. New York, NY, USA: Wiley, 1997, pp. 852–858.

[21] F. H. Larsen, "Probe correction of spherical near-field measurements," *Electron. Lett.*, vol. 13, no. 14, pp. 393–395, 1977.

[22] T. A. Laitinen, S. Pivnenko, and O. Breinbjerg, "Odd-order probe correction technique for spherical near-field antenna measurements," *Radio Sci.*, vol. 40, no. 3, pp. 1–11, 2005.

[23] G. Hindman and D. Fooshe, "Probe correction effects on planar, cylindrical and spherical near-field measurements," in *AMTA Annu. Meeting & Symp.,* Oct. 1998.

[24] C. Taybi, M. A. Moutaouekkil, K. K. Rodrigues, B. Elmagroud, and A. Ziyyat, "Probes correction for planar near field antennas measurements," in *Proc. IEEE 15th Mediterr. Microw. Symp. (MMS)*, Lecce, Italy, 2015, pp. 1–4.

[25] S. Hisatake, G. Kitahara, K. Ajito, Y. Fukada, N. Yoshimoto, and T. Nagatsuma, "Phase-sensitive terahertz self-heterodyne system based on photodiode and low-temperature-grown GaAs photoconductor at 1.55 μm," *IEEE Sensors J.*, vol. 13, no. 1, pp. 31–36, Jan. 2013.

[26] S. Hisatake and T. Nagatsuma, "Nonpolarimetric technique for homodyne-type electrooptic field detection," *Appl. Phys. Exp.*, vol. 5, no. 1, Dec. 2011, Art. no. 012701.

[27] H. Togo, A. Sasaki, A. Hirata, and T. Nagatsuma, "Characterization of millimeter-wave antenna using photonic measurement techniques," *Int. J. RF Microw. Comput.-Aided Eng.*, vol. 14, no. 3, pp. 290–297, 2004.

[28] H. H. N. Pham, S. Hisatake, and T. Nagatsuma, "Characterization of an F-band horn antenna based on electro-optic near-field measurements," *IEICE Trans. Electron.*, vol. E98.C, no. 8, pp. 866–872, 2015.

[29] T. Nagatsuma, S. Hisatake, and H. H. N. Pham, "Photonics for millimeter-wave and terahertz sensing and measurement," *IEICE Trans. Electron.*, vol. E99.C, no. 2, pp. 173–180, 2016.

[30] S. Hisatake, "Electrooptic field visualization and its application to millimeter-wave and terahertz antenna characterization," in *Proc. IEEE Conf. Antenna Meas. Appl. (CAMA)*, Tsukuba, Japan, 2017, pp. 330–333.

[31] H. Takeuchi and S. Hisatake, "Microwave signal detection based on the nonpolarimetric frequency down-conversion technique," *IEEE Sens. Lett.*, vol. 4, no. 9, pp. 1–4, Sep. 2020.

[32] J. J. Lee, E. M. Ferren, D. P. Woollen, and K. M. Lee, "Near-field probe used as a diagnostic tool to locate defective elements in an array antenna," *IEEE Trans. Antennas Propag.*, vol. 36, no. 6, pp. 884–889, Jun. 1988.

[33] A. C. Newell, "Error analysis techniques for planar near-field measurements," *IEEE Trans. Antennas Propag.*, vol. 36, no. 6, pp. 754–768, Jun. 1988.

[34] M. M. Leibfritz and P. M. Landstorfer, "Full probe-correction for near-field antenna measurements," in *Proc. IEEE Antennas Propag. Soc. Int. Symp.*, Albuquerque, NM, USA, 2006, pp. 437–440.